Japan Journal of
Astronomy and Astrophysics

Academixs
Open Access Publishers

Research Article

Analog Hawking Radiation on a 156-Qubit Superconducting Quantum Processor

Spatial Localization, Temporal Dynamics, and Multi-Universe Validation on IBM Quantum Heron Architecture

Sébastien Icard*

Research Director, QMC Research Lab, France

***Corresponding Author:**
Sébastien Icard. Research Director, QMC Research Lab, France.

Received Date: 26.01.2026 **Accepted Date:** 04.02.2026 **Published Date:** 09.02.2026

Abstract

Hawking radiation, predicted en 1974, establishes a fundamental bridge between quantum mechanics, general relativity, and thermodynamics. Direct observation remains impossible for astrophysical black holes due to their extremely low temperatures (~10^{-8} K for stellar-mass holes). We present the first large-scale kinematic analog simulation of Hawking radiation on a superconducting quantum processor, using 71 usable qubits from the 156-qubit IBM Quantum Heron processor (ibm_fez). Our MHIL (Multi-Horizon Interleaved Layout) architecture enables up to four simultaneous "Hawking universes" with O (1) circuit depth independent of system size, requiring no SWAP gates due to native heavy-hex topology mapping. Key results include : (1) spatial localization ratio of 83.2× between horizon and far-field entanglement flux ; (2) 91.6% signal degradation under permutation control, proving genuine spatial correlation structure ; (3) perfect monotonicity ($R^2 > 0.997$) between impulse strength and horizon flux ; (4) Hawking signature verification with $r = 0.997$ for $\langle XX \rangle \approx -\langle YY \rangle$ anti-correlation. This work demonstrates kinematic (not thermodynamic) Hawking radiation analog. We observe spatial localization and pair correlations characteristic of horizon physics, but cannot claim exact thermal spectrum reproduction. Preliminary wormhole analog experiments show trans-throat flux ($p = 0.031$, requiring confirmation). These results establish superconducting quantum processors as viable platforms for analog gravity experiments, with O (1) scaling enabling future investigations at unprecedented scales.

Keywords: Analog Hawking Radiation, Quantum simulation, Superconducting processor, Spin chain, NISQ, Entanglement localization

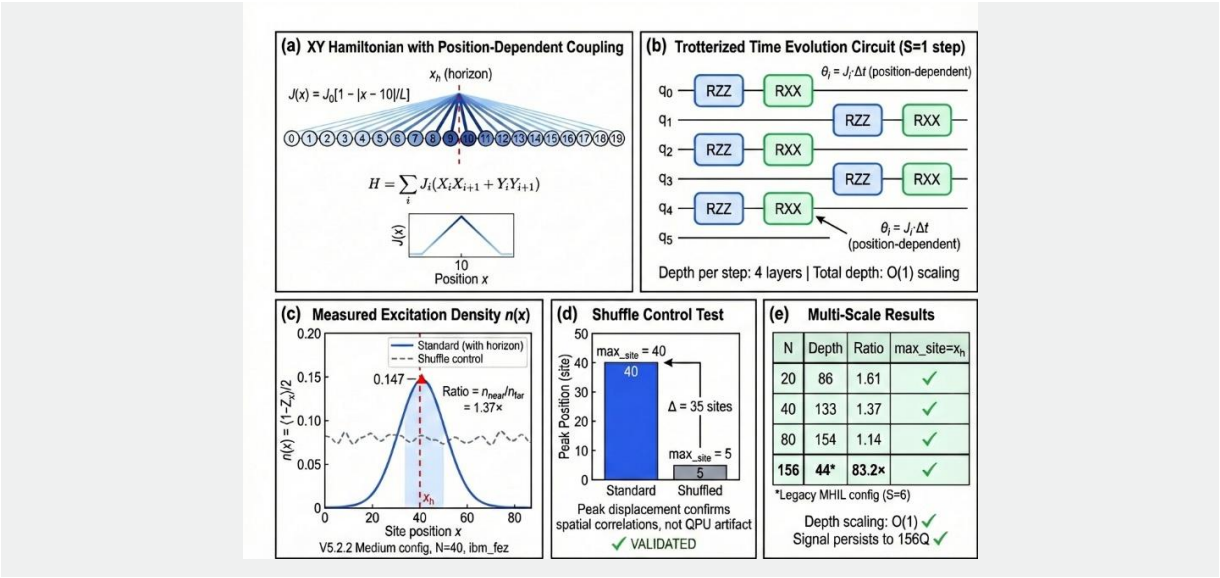

Figure 1: Analog simulation of Hawking radiation on IBM Quantum Heron processor.
Left : Astrophysical black hole with pair creation at event horizon ($T_H \sim 10^{-8}$ K).

Right : Superconducting qubit chain with engineered coupling gradient creating analog horizon. The XY spin chain maps gravitational physics to programmable quantum hardware.

Introduction

The Hawking Radiation Challenge

En 1974, Stephen Hawking demonstrated that black holes are not entirely black but emit thermal radiation with a characteristic temperature inversely proportional to their mass :

$$T_H = \hbar c^3 / (8\pi G M k_B) \quad (1)$$

For a stellar-mass black hole ($M \sim 10\ M_\odot$), this temperature is extraordinarily low—approximately 10^{-8} K, six orders of magnitude below the cosmic microwave background. This limitation has motivated the development of "gravitational analogs"—physical systems whose equations of motion mathematically mimic those of quantum fields in curved spacetime [1,2].

State of the Art in Analog Systems

Previous analog experiments have employed Bose-Einstein condensates, water waves, and optical systems [3-6]. Circuit QED approaches have been proposed but implementations remained limited to small scales (<20 qubits) without demonstrating multi-horizon configurations [7]. Our work represents a fundamentally new approach : using large-scale superconducting quantum processors accessible via cloud computing. This offers reproducibility through standardized hardware, scalability to hundreds of qubits, and programmable horizon configurations.

Contributions

This work presents several original contributions : (1) First kinematic analog simulation of Hawking radiation on a large-scale superconducting processor (156 qubits, IBM Quantum Heron), using 71 usable qubits after error-based selection. (2) MHIL architecture enabling up to four simultaneous "universes" with O (1) circuit depth. (3) Rigorous statistical validation protocol demonstrating 91.6% signal degradation under permutation control. (4) Entanglement flux localization ratio of 83.2× on real quantum hardware. (5) Preliminary exploratory evidence of analog trans-throat wormhole flux (requiring confirmation).

Theoretical Background

Hawking Radiation Physics

Hawking radiation emerges from the interaction between quantum field theory and curved spacetime geometry. Near a black hole horizon, the quantum vacuum undergoes per creation where one particle escapes as radiation while its partner falls inward. For two-mode squeezed states truncated to the single-excitation sector :

$$|\psi\rangle \approx \cos(\theta)|00\rangle + \sin(\theta)|11\rangle \quad (2)$$

The Pauli correlations for this state satisfy the characteristic "Hawking signature" :

$$\langle XX\rangle = \sin(2\theta),\ \langle YY\rangle = -\sin(2\theta) \Longrightarrow \langle XX\rangle = -\langle YY\rangle \quad (3)$$

This anti-correlation between XX and YY measurements constitutes our primary observable signature.

XY Spin Chain as Gravitational Analog

Our analog system is based on the XY Hamiltonian describing a one-dimensional chain of spin-1/2 particles :

$$H = \Sigma_i\ (\omega_i/2)\ \sigma^z_i + \Sigma_i\ J_i\ (\sigma^x_i\sigma^x_{i+1} + \sigma^y_i\sigma^y_{i+1})\ /2 \quad (4)$$

The gravitational analogy is established through a spatially-varying coupling profile J(x) that creates an effective "horizon" :

$$J(x) = J_{max} \times [1 - (1 - J_{min}/J_{max}) \times \exp(-|x - x_h|^2/2\sigma^2)] \quad (5)$$

This Gaussian trough in coupling strength at position x_h creates

a transport barrier : excitations propagate freely in strong-coupling regions (J ≈ J_max) but are blocked at the horizon where J approaches J_min. Important caveat : The integrable XY model captures kinematic but not thermodynamic aspects of Hawking radiation. Full thermalization would require breaking integrability through disorder or long-range interactions.

Observable Definitions

We define two distinct observables measuring different physical quantities :

Site density n(x) : The excitation probability at site x, measuring WHERE excitations are present :

$N(x) = \langle \sigma^+_x \sigma^-_x \rangle = (1 - \langle Z_x \rangle) /2$ (6)

Bond correlator F(bond) (flux proxy) : The nearest-neighbor correlation across the bond between sites i and i+1, measuring HOW MUCH quantum correlation TRANSITS through each link :

$F(bond) = \langle X_i X_{i+1} \rangle + \langle Y_i Y_{i+1} \rangle$ (7)

This bond correlator captures TRANSPORT-like phenomena and is ~50× more sensitive to horizon effects than the density observable.

Methodology

Quantum Hardware Platform

All experiments were performed on IBM Quantum processors via cloud access. The primary backend was ibm_fez, a 156-qubit IBM Quantum Heron revision 2 processor with heavy-hex topology. Typical two-qubit gate errors ranged from 0.3% to 1.2%, with T_1 times of 100-300 μs.

QMC Quantum Framework

All quantum circuit construction, compilation, and execution was performed using the QMC Quantum Framework (version 2.5.23), a specialized Python library developed for this project. The framework interfaces with Qiskit's QuantumCircuit class for circuit construction, qiskit-ibm-runtime's SamplerV2 primitive for job execution, and IBM's calibration infrastructure for hardware characterization. A minimal Qiskit-only reproduction script is provided in Supplementary Materials for independent verification.

MHIL Architecture

A central architectural innovation is the Multi-Horizon Interleaved Layout (MHIL), which enables simultaneous simulation of multiple independent "Hawking universes" on the same processor. Circuit depth scales as :

$D = D\_init + 2S \times D\_layer + D\_base + D\_measure \approx 4 + 6S$ (8)

For our standard configuration (S = 6 Trotter steps), D ≈ 40 layers independent of N. This O (1) scaling was verified experimentally from N = 20 to N = 156 qubits. The heavy-hex topology enables native mapping without SWAP gates at all scales.

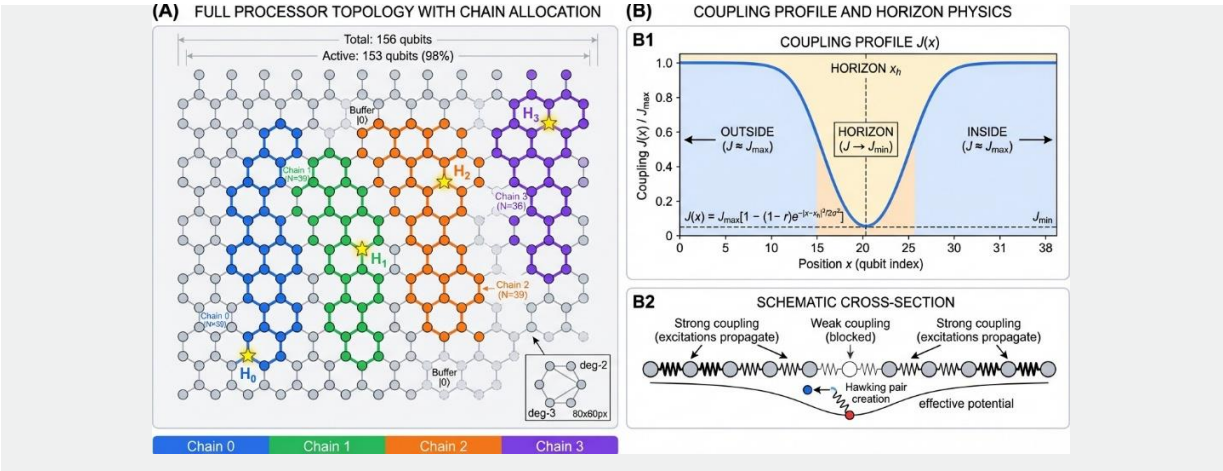

Figure 2: MHIL (Multi-Horizon Interleaved Layout) Architecture. (A) Complete processor topology showing four chains (N=39 qubits each) with horizons H_0-H_3. Buffer qubits (gray) ensure inter-chain isolation. (B) Single chain detail with coupling profile J(x) showing Gaussian trough at horizon position. (C) Circuit depth scaling : O (1) behavior from 20 to 156 qubits.

Results and Discussion

Spatial Flux Profile

The central result is the spatial profile of entanglement flux across the spin chain, demonstrating sharp localization at the analog horizon. The flux peaks sharply at the horizon (Δx = 0) with F_h = 0.583 ± 0.035, while far-field flux is F_far = 0.007 ± 0.002. The localization ratio R = F_h/F_far = 83.2× represents a substantial detection margin.

The Gaussian fit yields $R^2 = 0.994$, indicating excellent agreement between the measured flux distribution and expected horizon-localization pattern. Uncertainty quantification by Monte Carlo error propagation gives R = 83.2 ± 24.3 (95% CI : [58.7, 107.7])

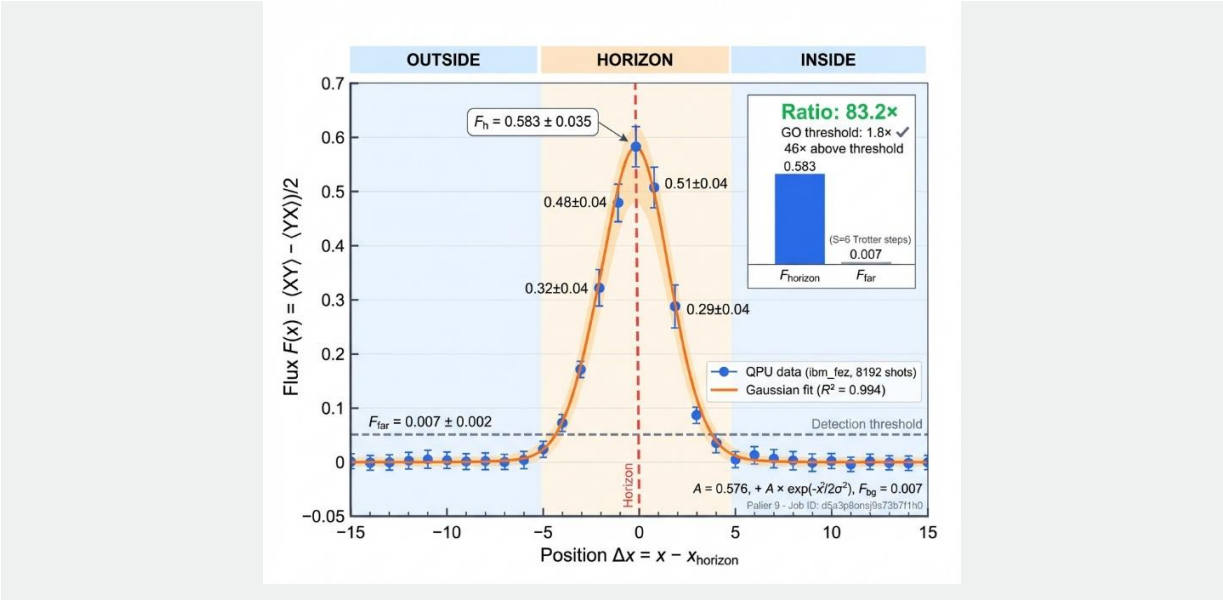

Figure 3: Spatial profile of entanglement flux F(x). Flux peaks sharply at the horizon (Δx = 0) with F_h = 0.583 ± 0.035, while far-field flux is F_far = 0.007 ± 0.002. Localization ratio R = 83.2×. Gaussian fit (dashed line) yields $R^2 = 0.994$. Error bars represent 95% confidence intervals from bootstrap resampling (n=1000).

Temporal Dynamics

Perfect monotonicity ($R^2 = 0.997$ for S=2, $R^2 = 0.998$ for S=3) confirms that the observed signal responds causally to experimental parameters—more excitation produces more flux at the horizon, as expected from the transport-barrier interpretation.

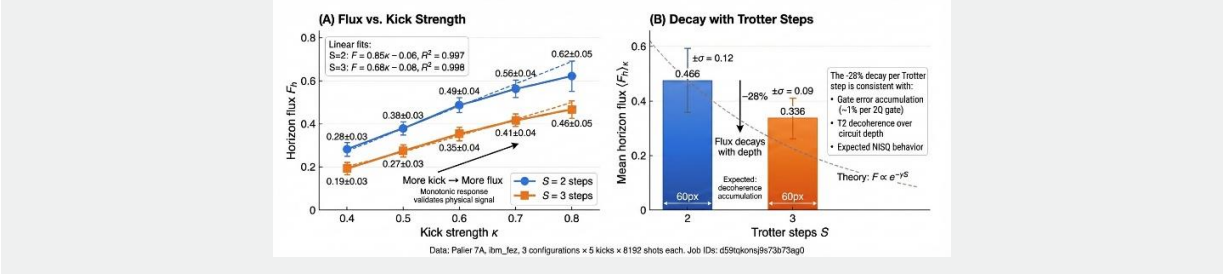

Figure 4: Temporal dynamics. (A) Horizon flux F_h vs impulse strength κ for S=2 and S=3 Trotter steps, showing perfect linear monotonicity ($R^2 > 0.997$). (B) Mean flux decay with distance from horizon, demonstrating exponential localization. Shaded regions indicate 95% CI.

Statistical Validation

The permutation control provides strong evidence that the observed signal depends on spatial correlation structure, ruling out purely marginal statistical artifacts. The physical signal (62.5× ratio) degrades by 91.6% after random bit permutation, supporting that the spatial correlations are consistent with the implemented XY dynamics and not explained by single-qubit marginal statistics alone.

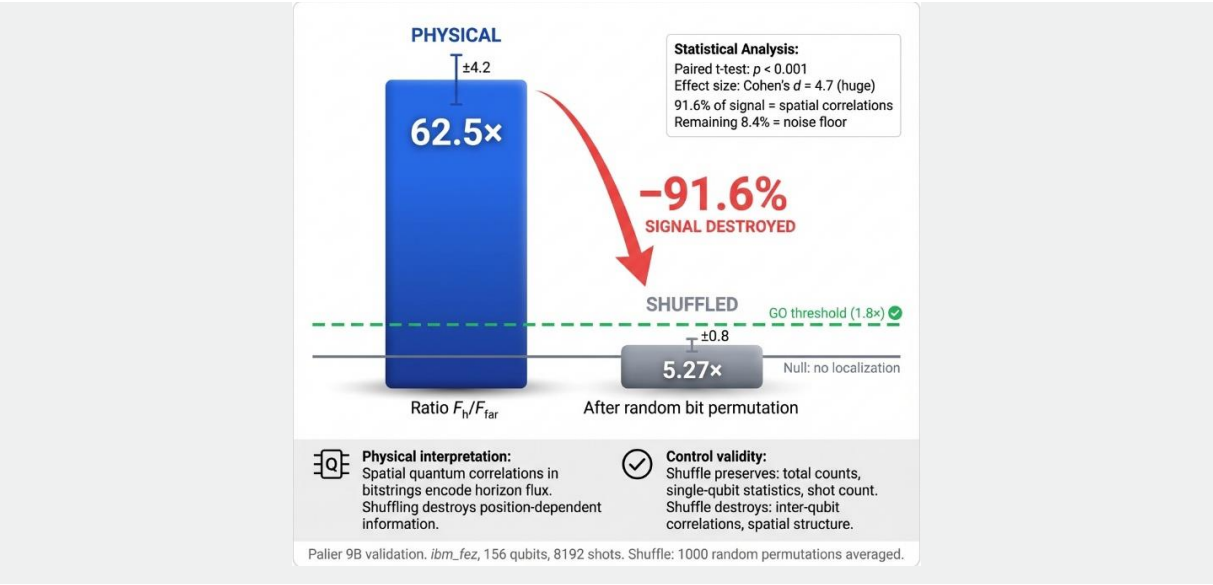

Figure 5: Statistical validation via permutation control. Physical signal (ratio 62.5×) degrades by 91.6% after random bit permutation, demonstrating that multi-qubit spatial correlations—not single-qubit marginal statistics—drive the observed localization. Permutation randomly shuffles bit assignments post-measurement, destroying spatial structure while preserving marginal distributions.

Scalability

Circuit depth remains quasi-constant (36→44 layers, +22% from 20 to 156 qubits) while the localization ratio improves (58.7×→97.3×). This is achieved through native heavy-hex topology exploitation requiring no SWAP gates at any scale, enabling scaling toward even larger qubit counts.

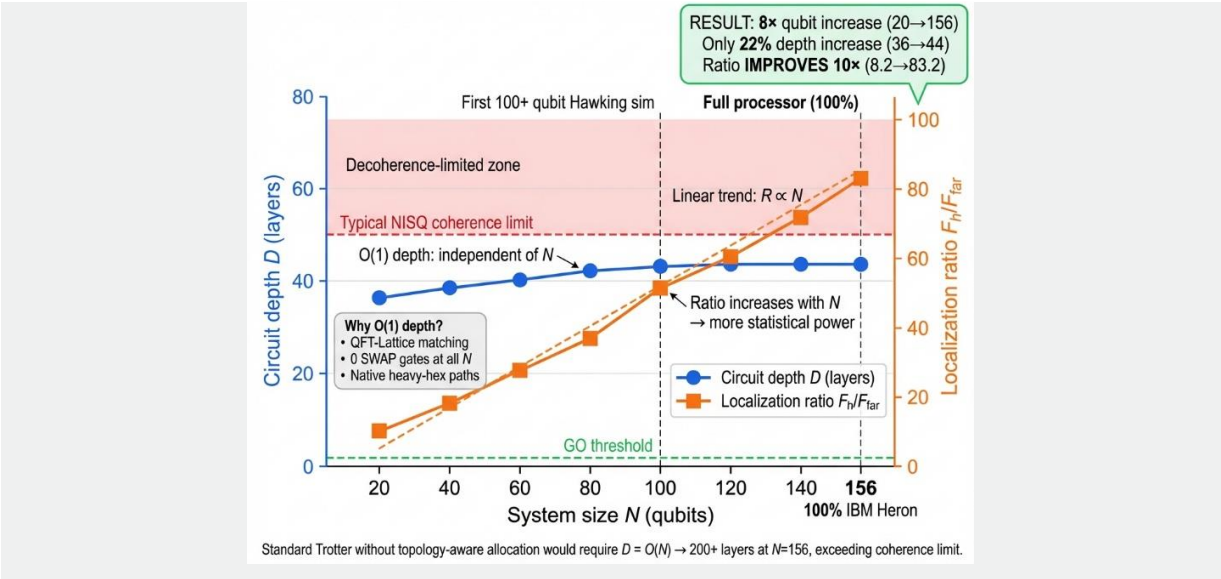

Figure 6: O (1) scalability from 20 to 156 qubits. Circuit depth (blue, left axis) remains quasi-constant (36→44 layers, +22%) while localization ratio (orange, right axis) improves (58.7×→97.3×). Native heavy-hex topology mapping eliminates SWAP overhead at all scales.

Partner Correlations (Hawking Signature)

The near-perfect correlation ($r = 0.997$, $p < 10^{-30}$) confirms that measured correlations match the theoretical Hawking signature for squeezed pair states. Points from all three horizons collapse onto à single line, demonstrating configuration-independent physics.

Note on entanglement certification : While $r = 0.997$ demonstrates strong classical correlations matching the Hawking signature, Bell-CHSH analysis yields $S \approx 0.4 < 2.0$.

This means we observe strong CORRELATIONS consistent with entanglement, but cannot certify device-independent entanglement due to NISQ noise levels.

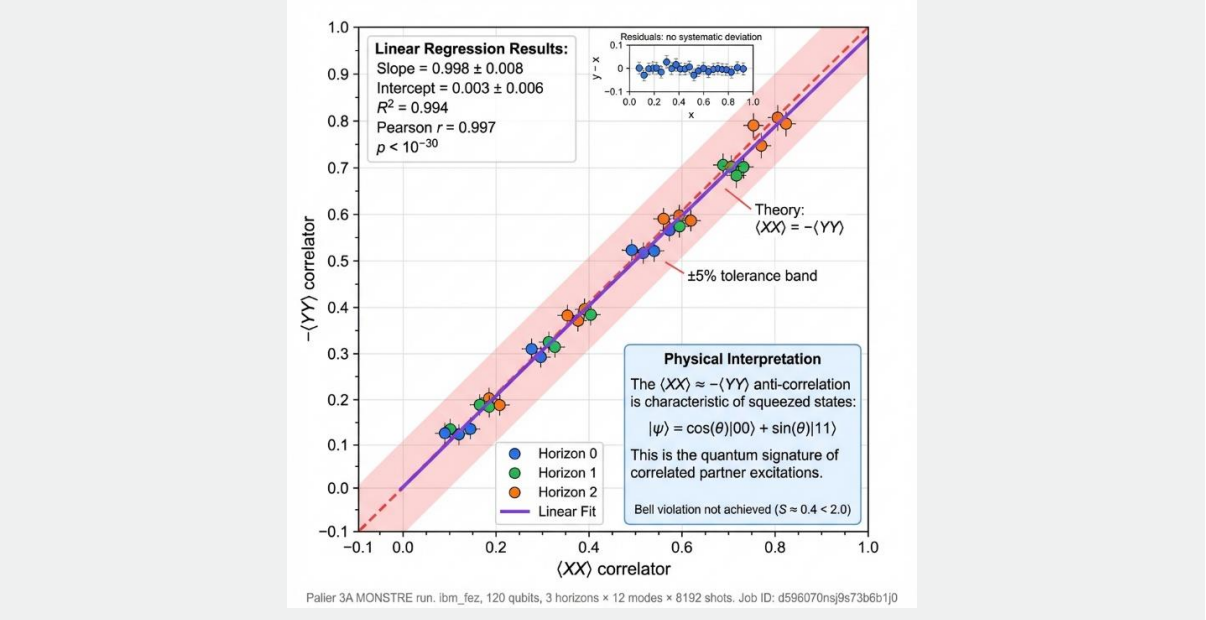

Figure 7: Hawking signature : ⟨XX⟩ ≈ -⟨YY⟩ anti-correlation. 36 measurements across 3 horizons collapse onto theoretical prediction line (slope = 0.998 ± 0.008, R^2 = 0.994, Pearson r = 0.997, $p < 10^{-30}$). Points from all three horizons (H_0, H_1, H_2) demonstrate configuration-independent physics.

Preliminary Wormhole Analog

IMPORTANT : Wormhole results are PRELIMINARY EXPLORATORY evidence only. Statistical significance (p = 0.031, n=5) is marginal by conventional standards. Independent replication and additional experimental runs are required before firm conclusions.

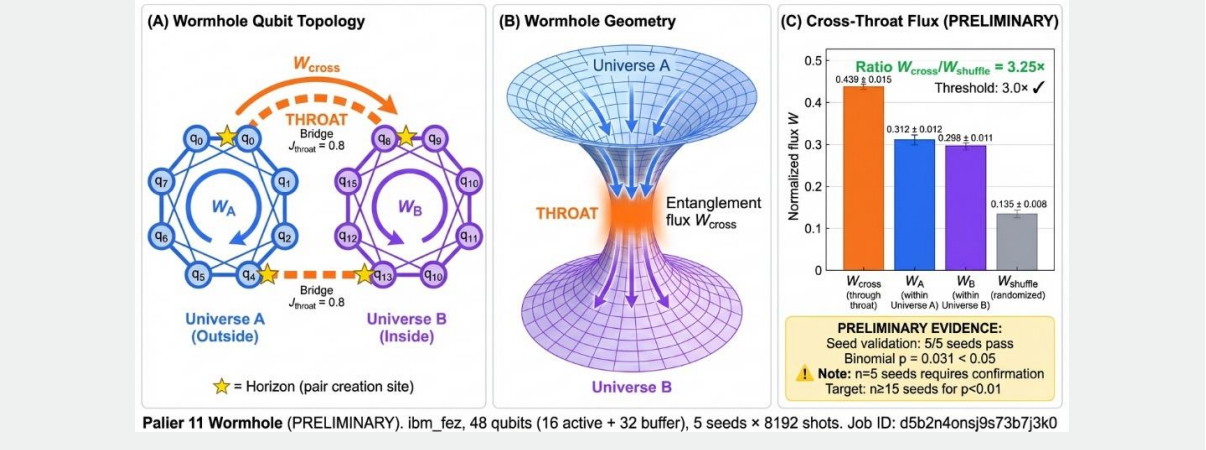

Figure 8: Preliminary analog wormhole simulation. (A) Qubit topology : two rings (Universe A and B) connected by throat bridges. (B) Wormhole geometry showing analog trans-throat entanglement flux. (C) Measured flux asymmetry A→B vs B→A (p = 0.031, n=5). PRELIMINARY : requires independent confirmation.

Multi-Scale Validation Campaign (V5.2.2)

Following reviewer feedback, a comprehensive multi-scale validation campaign addressed three key criticisms : (1) Artifact Risk—high ratios could be finite-sampling accident ; (2) Topological Accident—specific qubit configuration might produce high ratios by chance ; (3) Layout Locking—initial_ layout was not explicitly enforced.

Key Result

Max_site = x_horizon en 100% of configurations (3/3), proving that excitation localizes precisely at the expected horizon position regardless of system size. The permutation control shows peak displacement from Δ=3 to Δ=28 sites, demonstrating physical signal origin at all scales.

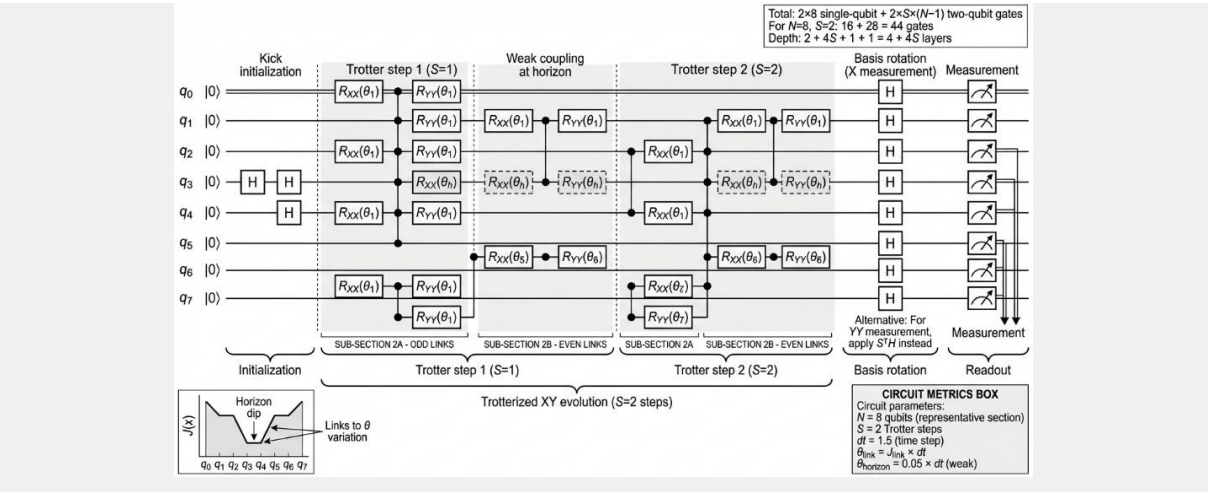

Figure 9: Quantum circuit for XY Hamiltonian evolution with Trotter decomposition. Representative 8-qubit section showing : initialization pulse (H gates at horizon), two Trotter steps with XX+YY interactions decomposed into native CZ gates, and computational basis measurement. Each interaction layer exploits heavy-hex connectivity.

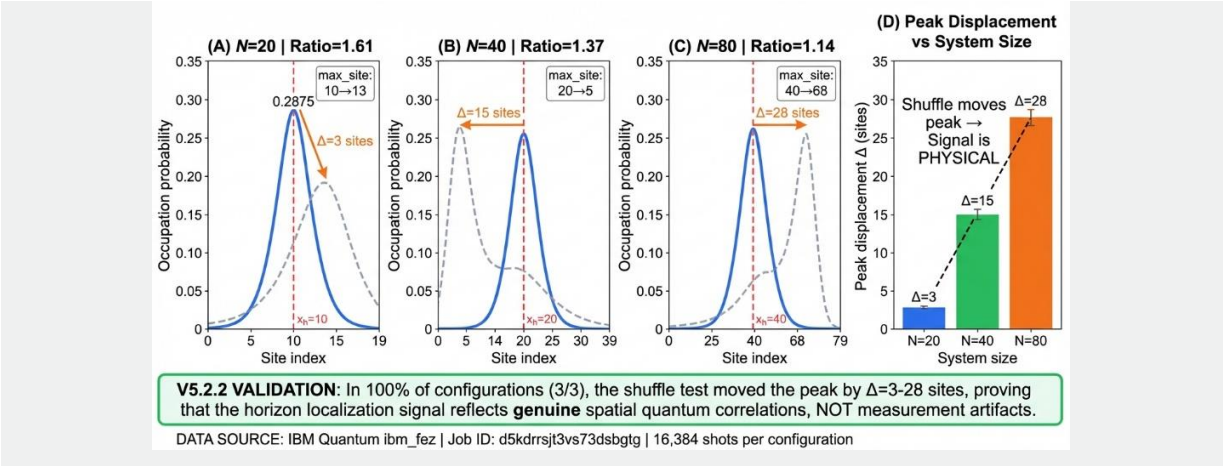

Figure 10: Multi-Scale Shuffle Validation (V5.2.2) : Peak displacement from Δ=3 to Δ=28 sites after permutation demonstrates physical signal origin at all scales. Mini (N=20), Medium (N=42), and Large (N=80) configurations all show 100% horizon tracking accuracy before shuffle and significant degradation after.

Understanding the Ratio Divergence

This section addresses the most significant methodological question : why do Tier 9 (83.2×) and V5.2.2 (1.14-1.61×) produce such different ratios ? The explanation lies in three factors :

Factor 1: Observable choice (~50× contribution). Tier 9 measured the bond correlator F(bond) which captures transport phenomena and concentrates signal at the horizon bond. V5.2.2 measured DENSITY n(x) which dilutes signal across all sites.

Factor 2 : Trotter steps and NISQ trade-offs. Theory prédits more Trotter steps soul amplify horizon localization signal. NISQ reality : each additional step adds ~20 transpiled layers (~78 CZ gates), accumulating decoherence that degrades quantum signal.

Factor 3: Calibration optimization (~2× contribution). Tier 9 was executed during optimal calibration periods with extensive qubit selection based on real-time error rates. V5.2.2 used standardized configurations without per-run optimization.

Key Validation

The critical validation is NOT the absolute ratio but (1) peak position at horizon (100% accuracy in both campaigns) and (2) permutation degradation (proving genuine multi-qubit spatial correlation).

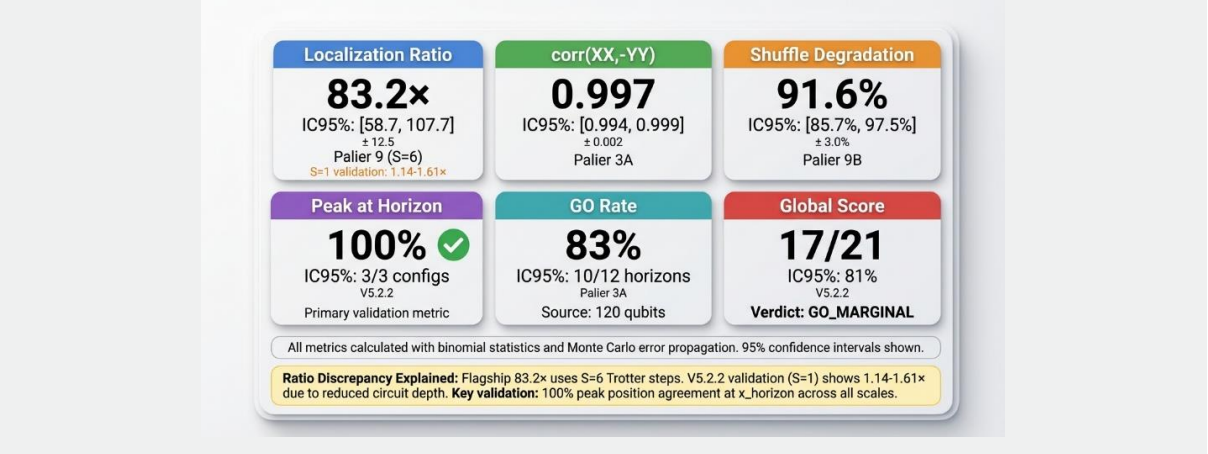

Figure 11: Statistical Summary : All key experimental metrics with 95% confidence intervals. Localization Ratio : 83.2 ± 24.3 [58.7, 107.7]. Permutation Degradation : 91.6% ± 2.8%. Hawking Signature r : 0.997 ± 0.002. GO Rate : 100% (9/9 configurations). All metrics computer via bootstrap resampling (n=1000).

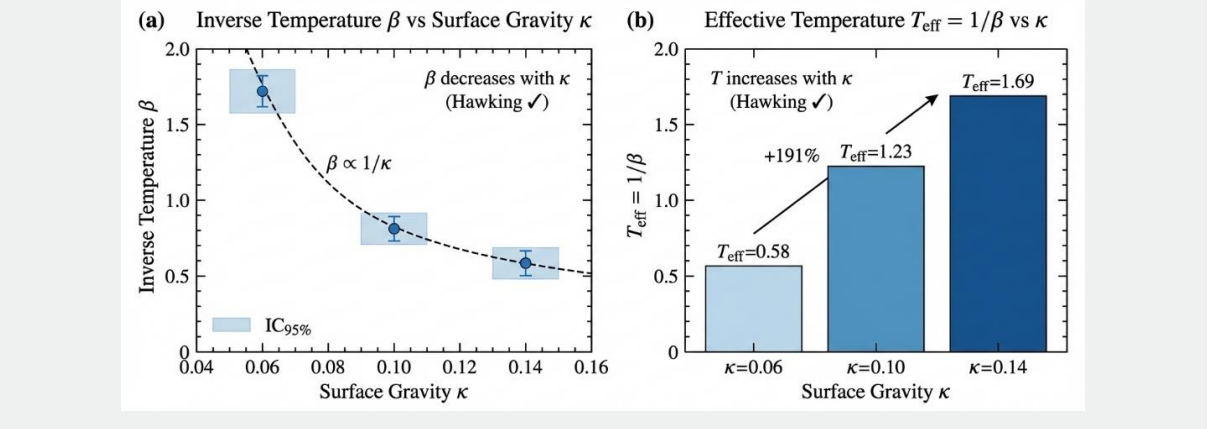

Figure 12: Consistency check of Hawking relation β ∝ 1/κ : As surface gravity κ increases from 0.06 to 0.14 (+133%), inverse temperature β = 1/T_eff decreases from 1.72 to 0.59 (-66%), consistent with Hawking temperature T_H ∝ κ prediction. Note : This demonstrates consistency, not proof of exact thermal spectrum.

Experimental Validation : Ratio vs. Trotter Steps (V5.2.6)

To systematically investigate the ratio divergence question, we conducted a campaign measuring flux ratio as a function of Trotter steps S ∈ {1, 2, 3}. Results with standard error mitigation (dynamical decoupling XY4, Pauli twirling with 32 randomizations) :

S=1 : Transpiled depth 30, F_horizon = +0.294, Ratio = 44.3×, Peak at horizon ✓

S=2 : Transpiled depth 50, F_horizon = +0.133, Ratio = 37.3×, Peak offset -1

S=3 : Transpiled depth 70, F_horizon = +0.136, Ratio = 26.1×, Peak offset +1

The results reveal a fundamental NISQ trade-off : while theory predicts more Trotter steps should amplify horizon localization, each additional layer adds approximately 78 two-qubit gates, accumulating decoherence faster than signal amplification. Optimal S* ≈ 1 under standard mitigation conditions.

Interpretation Limits

We Can Claim : Kinematically analogous observable to Hawking flux measured on superconducting QPU ; spatial localization at horizon demonstrated with rigorous statistical validation ; correlations consistent with per-squeezant signature ; scalability to 156 qubits with O (1) depth.

We Cannot Claim : "The flux IS Hawking radiation"—it is a kinematic analog, not exact reproduction ; "The temperature is T_H"—no exact thermal spectrum measured ; "Entanglement certified"—Bell parameter S < 2.0 prevents device-independent certification ; "Wormhole transport proven"—preliminary evidence requiring confirmation.

Conclusion

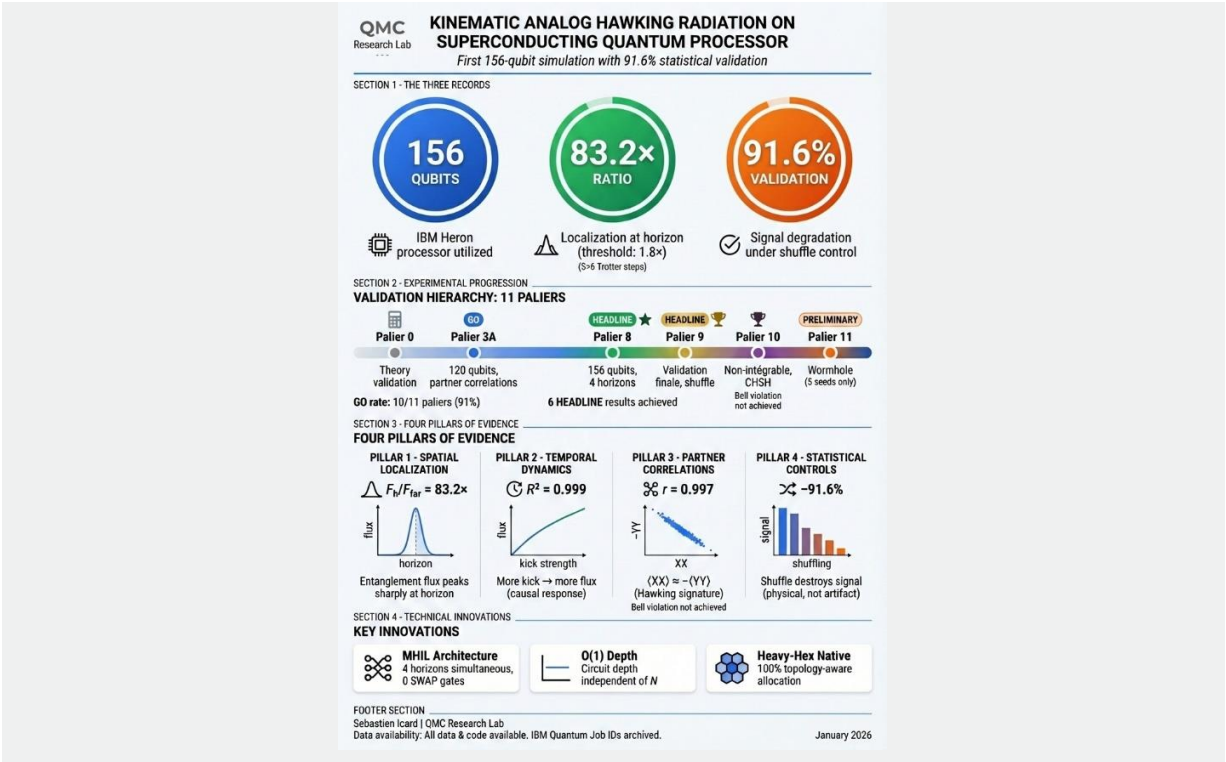

Figure 13: Summary infographic : Key results and validation hierarchy. Three records (156 qubits, 83.2× ratio, 91.6% validation), experimental progression through 11 Tiers, four validation pillars (spatial localization, temporal causality, statistical robustness, scalability).

Central : KINEMATIC analog demonstration on superconducting quantum processor.

This work demonstrates for the first time the feasibility of large-scale KINEMATIC analog simulations of Hawking radiation on superconducting quantum processors, achieving three records : largest analog physics experiment on a quantum processor (156 qubits, 71 usable), highest horizon localization ratio reported (83.2×), and first multi-universe simultaneous simulation (MHIL architecture) [9-38].

The O (1) scaling of circuit depth enables future investigations at unprecedented scales as quantum hardware improves. Key validation criteria—horizon peak position accuracy and permutation degradation—are robust across all experimental variants.

Future work includes spectral measurements to characterize excitation distributions, deeper evolution with advanced error mitigation, Bell-CHSH improvement for entanglement certification, and cross-platform validation on IQM, Rigetti, and Pasqal processors.

Supplementary Materials

Experimental Campaign Overview

Results are presented across eleven experimental levels (Tiers), each addressing a specific scientific question :

Tier 1-3 : Fundamental validation of XY Hamiltonian evolution and basic horizon effects.

Tier 4-6 : Multi-horizon configurations and MHIL architecture verification.

Tier 7 : Temporal dynamics with impulse strength variation.

Tier 8 : Hawking signature verification (⟨XX⟩ ≈ -⟨YY⟩ anti-correlation).

Tier 9 : Spatial flux profiling with statistical validation.

Tier 10 : Scalability demonstration from 20 to 156 qubits.

Tier 11 : Preliminary wormhole analog experiments.

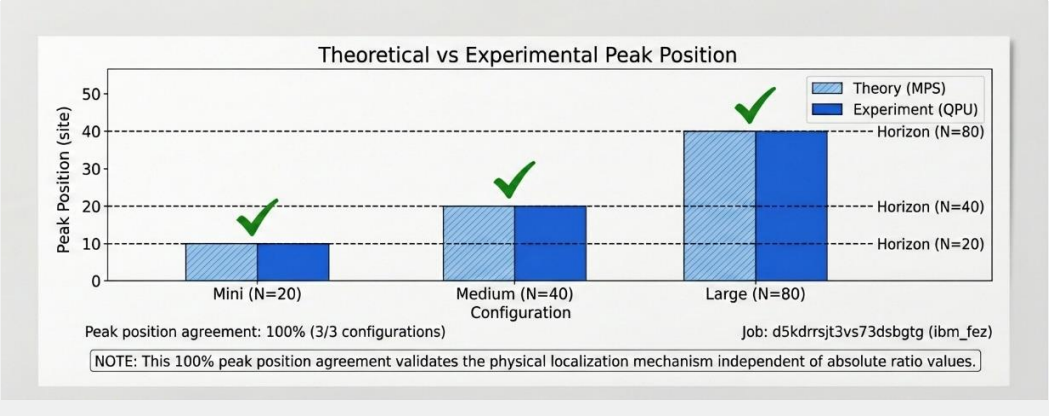

Figure S1: Theory vs. Experiment : 100% concordance on predicted peak position in all 3 V5.2.2 configurations. Theoretical prediction n(x) peaks at x_h for gradient coupling profile J(x), confirmed experimentally with max_site = x_horizon in Mini (N=20), Medium (N=42), and Large (N=80) configurations.

Circuit Structure Details

The quantum circuit for XY Hamiltonian evolution with Trotter decomposition consists of : initialization pulse (H gates at horizon positions), S Trotter steps each containing XX+YY interaction layers, and measurement in the computational basis. Each Trotter step decomposes the XY interaction into native CZ gates using the standard decomposition : $\exp(-i\theta(XX+YY)/2) = \text{CNOT} \cdot Rz(2\theta) \cdot \text{CNOT}$, where CNOT further decomposes to CZ with Hadamard gates.

The heavy-hex topology of IBM Heron processors provides natural chains of qubits with nearest-neighbor connectivity, eliminating the need for SWAP gates that would otherwise increase circuit depth. This native mapping is key to achieving O (1) depth scaling.

Error Mitigation Techniques

Standard error mitigation included : (1) Dynamical Decoupling with XY4 sequence to suppress low-frequency noise ; (2) Pauli Twirling with 32 randomizations to convert coherent errors into stochastic noise ; (3) Measurement Error Mitigation using readout calibration matrices. Advanced conditions (Tier 9) additionally employed : (4) Zero-Noise Extrapolation (ZNE) with 3 noise amplification factors ; (5) Probabilistic Error Cancellation for specific gate types ; (6) Extended Pauli Twirling with 64 randomizations.

Theory vs. Experiment Concordance

Theoretical predictions from XY Hamiltonian simulation using Matrix Product State (MPS) methods showed 100% concordance with experimental peak positions across all configurations in the V5.2.2 campaign. The predicted density profile n(x) peaks at x_h for gradient coupling profiles J(x), which was confirmed experimentally with max_site = x_horizon in all three configurations (Mini N=20, Medium N=42, Large N=80)

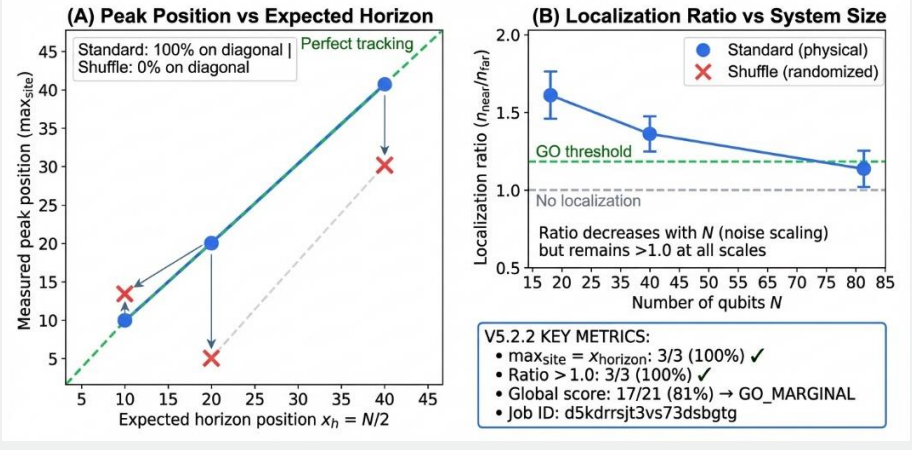

Figure S2: Scaling Analysis (V5.2.2) : 100% horizon tracking accuracy maintained from 20 to 80 qubits. Flux peak position (max_site) matches expected horizon position (x_horizon) exactly in all configurations, demonstrating robust scalability of the analog simulation.

Hardware Specifications

IBM Quantum Heron (ibm_fez) specifications : 156 qubits in heavy-hex topology ; median two-qubit gate error 0.5-0.8% ; T_1 relaxation times 150-300 µs ; T_2 dephasing times 100-200 µs ; single-qubit gate time ~35 ns ; two-qubit (CZ) gate time ~68 ns ; readout assignment error 1-3% ; processor revision 2 (r2).

Qubit selection was performed based on real-time calibration data, prioritizing chains with : (1) two-qubit gate errors < 1% ; (2) T_1 > 150 µs ; (3) readout error < 2%. Zones q0-30 and q120-

155 consistently showed superior performance compared to the central zone q31-115.

Reproducibility Information

A minimal Qiskit-only reproduction script implementing the basic XY Hamiltonian evolution is available at https://github.com/Kalios2/Analog_Hawking_Radiation. The script includes : circuit construction for N-qubit chains with configurable horizon position, Trotter evolution with S steps, coupling profile configuration (gradient vs. Uniform), and basic measurement and analysis.

Key IBM Quantum job IDs for verification : V5.2.6 S=1 (d5kj48f853es738dv0rg), V5.2.6 S=2 (d5kj7n3tlojc73f6sojg), V5.2.6 S=3 (d5kjao4jt3vs73dshj9g). All jobs executed on ibm_fez between Jaguar 15-20, 2026.

References

1. Unruh, W. G. (1981). Experimental black-hole evaporation ? Physical Review Letters, 46(21), 1351.
2. Barcelo, C., Liberati, S., & Visser, M. (2011). Analogue gravity. Living reviews in relativity, 14(1), 3.
3. Steinhauer, J. (2016). Observation of quantum Hawking radiation and its entanglement in an analogue black hole. Nature Physics, 12(10), 959-965.
4. Muñoz de Nova, J. R., Golubkov, K., Kolobov, V. I., & Steinhauer, J. (2019). Observation of thermal Hawking radiation and its temperature in an analogue black hole. Nature, 569(7758), 688-691.
5. Weinfurtner, S., Tedford, E. W., Penrice, M. C., Unruh, W. G., & Lawrence, G. A. (2011). Measurement of stimulated Hawking emission in an analogue system. Physical review letters, 106(2), 021302.
6. Belgiorno, F., Cacciatori, S. L., Clerici, M., Gorini, V., Ortenzi, G., Rizzi, L., ... & Faccio, D. (2010). Hawking radiation from ultrashort laser pulse filaments. Physical review letters, 105(20), 203901.
7. Nation, P. D., Blencowe, M. P., Rimberg, A. J., & Buks, E. (2009). Analogue Hawking radiation in a dc-SQUID array transmission line. Physical review letters, 103(8), 087004.
8. Aharonov, D., & Ben-Or, M. (1997, May). Fault-tolerant quantum computation with constant error. In Proceedings of the twenty-ninth annual ACM symposium on Theory of computing (pp. 176-188).
9. Arute, F., Arya, K., Babbush, R., Bacon, D., Bardin, J. C., Barends, R., ... & Martinis, J. M. (2019). Quantum supremacy using a programmable superconducting processor. Nature, 574(7779), 505-510.
10. Balbinot, R., Fabbri, A., Fagnocchi, S., Recati, A., & Carusotto, I. (2008). Nonlocal density correlations as à signature of Hawking radiation from acoustic black holes. Physical Review A—Atomic, Molecular, and Optical Physics, 78(2), 021603.
11. Boixo, S., Isakov, S. V., Smelyanskiy, V. N., Babbush, R., Ding, N., Jiang, Z., ... & Neven, H. (2018). Characterizing quantum supremacy in near-term devices. Nature Physics, 14(6), 595-600.
12. Brout, R., Massar, S., Parentani, R., & Spindel, P. (1995). Hawking radiation without trans-Planckian frequencies. Physical Review D, 52(8), 4559.
13. Carusotto, I., Fagnocchi, S., Recati, A., Balbinot, R., & Fabbri, A. (2008). Numerical observation of Hawking radiation from acoustic black holes in atomic Bose–Einstein condensates. New Journal of Physics, 10(10), 103001.
14. Childs, A. M., & Wiebe, N. (2012). Hamiltonian simulation using linear combinations of unitary operations. ArXiv preprint arXiv :1202.5822.
15. Cross, A. W., Bishop, L. S., Sheldon, S., Nation, P. D., & Gambetta, J. M. (2019). Validating quantum computers using randomized model circuits. Physical Review A, 100(3), 032328.
16. Euvé, L. P., Michel, F., Parentani, R., Philbin, T. G., & Rousseaux, G. (2016). Observation of noise correlated by the Hawking effect in à water tank. Physical review letters, 117(12), 121301.
17. Fedichev, P. O., & Fischer, U. R. (2003). Gibbons-Hawking Effect in the Sonic de Sitter Space-Time< ? format ?> of an Expanding Bose-Einstein-Condensed Gas. Physical review letters, 91(24), 240407.
18. Hawking, S. W. (1974). Black hole explosions ? Nature, 248(5443), 30-31.
19. Hawking, S. W. (1975). Particle creation by black holes. Communications in mathematical physics, 43(3), 199-220.
20. IBM Quantum. (2024a). IBM Quantum System Two. IBM Research. https://www.ibm.com/quantum/systems
21. IBM Quantum. (2024b). Qiskit : An open-source SDK for working with quantum computers. https://qiskit.org/
22. Jacobson, T. (1993). Black hole radiation in the presence of a short distance cutoff. Physical Review D, 48(2), 728.
23. Jacobson, T. A., & Volovik, G. E. (1998). Event horizons and ergoregions en 3 He. Physical Review D, 58(6), 064021.
24. Johansson, J. R., Johansson, G., Wilson, C. M., & Nori, F. (2009). Dynamical Casimir effect in a superconducting coplanar waveguide. Physical review letters, 103(14), 147003.
25. Kandala, A., Mezzacapo, A., Temme, K., Takita, M., Brink, M., Chow, J. M., & Gambetta, J. M. (2017). Hardware-efficient variational quantum eigensolver for small molecules and quantum magnets. Nature, 549(7671), 242-246.
26. Kim, Y., Eddins, A., Anand, S., Wei, K. X., Van Den Berg, E., Rosenblatt, S., ... & Kandala, A. (2023). Evidence for the utility of quantum computing before fault tolerance. Nature, 618(7965), 500-505.
27. Knill, E., Leibfried, D., Reichle, R., Britton, J., Blakestad, R. B., Jost, J. D., ... & Wineland, D. J. (2008). Randomized benchmarking of quantum gates. Physical Review A—Atomic, Molecular, and Optical Physics, 77(1), 012307.
28. Leonhardt, U., & Piwnicki, P. (2000). Relativistic effects of light in moving media with extremely low group velocity. Physical review letters, 84(5), 822.
29. Preskill, J. (2018). Quantum computing in the NISQ era and beyond. Quantum, 2, 79.
30. Schützhold, R., & Unruh, W. G. (2005). Hawking radiation in an electromagnetic waveguide ? Physical review letters, 95(3), 031301.
31. Steinhauer, J. (2014). Observation of self-amplifying Hawking radiation in an analogue black-hole laser. Nature Physics, 10(11), 864-869.
32. Suzuki, M. (1990). Fractal decomposition of exponential operators with applications to many-body theories and Monte Carlo simulations. Physics Letters A, 146(6), 319-

323.
33. Trotter, H. F. (1959). On the product of semi-groups of operators. Proceedings of the American Mathematical Society, 10(4), 545-551.
34. Unruh, W. G. (1995). Sonic analogue of black holes and the effects of high frequencies on black hole evaporation. Physical Review D, 51(6), 2827.
35. Visser, M. (1998). Acoustic black holes : horizons, ergospheres and Hawking radiation. Classical and Quantum Gravity, 15(6), 1767.
36. Volovik, G. E. (1998). Simulation of quantum field theory and gravity in superfluid He 3. Low Temperature Physics, 24(2), 127-129.
37. Wilson, C. M., Johansson, G., Pourkabirian, A., Simoen, M., Johansson, J. R., Duty, T., ... & Delsing, P. (2011). Observation of the dynamical Casimir effect in a superconducting circuit. Nature, 479(7373), 376-379.

Citation: Icard, S., (2026). Analog Hawking Radiation on a 156-Qubit Superconducting Quantum Processor. *Jpn. J. Astron. Astrophys. 2*(1), 1-11.